Hydraulic and thermal characterization of a family of thermo-hydraulic separators

Luca Toneatti[a,*], Marzio Piller[a], Dario Pozzetto[a], Elio Padoano[b], Marco Boscolo[b]

[a] Integrated Laboratory of ThermoHydraulic Applications, Dept. of Engineering and Architecture, University of Trieste, Via A. Valerio 10, 34127 Trieste (TS), Italy
[b] Dept. of Engineering and Architecture, University of Trieste, Via A. Valerio 10, 34127 Trieste (TS), Italy

HIGHLIGHTS

- Assessment of reliability of an over-simplified model of thermal-hydraulic separators.
- Disclosure of the complex flow- and temperature distribution within a separator.
- Marginal deviation from ideal operation mode.
- Assessment of thermal stratification within thermal-hydraulic separators.
- Thermal-hydraulic separation reduced at high flow ratio between connected circuits.

GRAPHICAL ABSTRACT

Isothermal surfaces within the device.

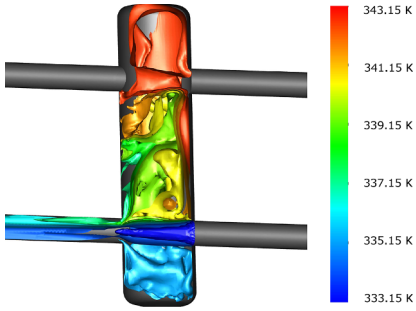

ARTICLE INFO

Keywords:
Thermal-hydraulic separator
Numerical simulation
Zero-dimensional model
Thermal stratification

ABSTRACT

Thermal-hydraulic separators (or hydraulic dispatchers) are flow collectors of relatively small size, connecting two or more hydraulic networks; they are mainly used to reduce the hydraulic interference of primary (e.g. heat supply) and secondary (e.g. heat consumer) circuits, thereby simplifying the system analysis, saving energy and operating complex hydraulic networks more safely. Hydraulic dispatchers are key components of modern district heating networks and of building water systems: nonetheless, little is known about their internal flow and temperature distribution and about their off-design performance.

The transfer of thermal energy from the primary to the secondary circuit is governed by the secondary-to-primary flow rate ratio and affected by the turbulent mixing within the device. A simple thermal model is commonly used for design purposes: it disregards the actual flow and temperature pattern within the device and relates the inflow and outflow temperature by neglecting the mixing of supply and return streams. This simple approach is potentially inaccurate under certain operating conditions (e.g. relatively high flow rates) and deserves a validation study.

Numerical simulations of flow and heat transfer are carried out, for a family of geometrically similar thermal-hydraulic separators under different operating condition. The reported numerical tests show that the aforementioned model is a reliable design tool under most operation conditions. Furthermore, it is verified that the device introduces a relatively modest pressure loss on the connected circuits, in particular when the flow rate ratio is close to one.

* Corresponding author at: Integrated Laboratory of ThermoHydraulic Applications, Dept. of Engineering and Architecture, Università degli Studi di Trieste, Via A. Valerio 10, 34127 Trieste (TS), Italy.
E-mail address: luca.toneatti@dia.units.it (L. Toneatti).

Accepted 2 July 2020

Nomenclature

Abbreviations

BIP, PIP, POP, BOP	Inflow/outflow openings, according to Table 1 and Fig. 1a
CCCP-DH	Central circulating pumps
DVSP-DH	Distributed variable speed pumps
HC	Heat consumer
HS	Heat source
THS	Thermal-hydraulic separator
TI	Turbulence intensity

Symbol

ΔT [K]	Temperature decay throughout the HC
$\dot{m}$ [kg·s^{-1}]	Mass-flow rate
c_p [J·kg^{-1}·K^{-1}]	Specific heat capacity of water
D [m]	Diameter of the barrel (Fig. 1a)
d [m]	Diameter of the connecting manifolds (Fig. 1a)
g [m·s^{-2}]	Gravitational acceleration magnitude
H [m]	Inter-axial distance between manifolds, connected to the same side of the THS (Fig. 1a)
k [W·m^{-1}·K^{-1}]	Thermal conductivity of water
P [Pa]	Gauge pressure, Eq. (2)
p [Pa]	Static pressure
SI [–]	Stratification index, Eq. (12)
t [s]	Time
T_1, T_2, T_3, T_4 [K]	bulk fluid temperatures at BIP, PIP, POP, BOP (see Table 1)
U [m·s^{-1}]	Mean inflow velocity through the BIP
u_τ [m·s^{-1}]	Friction velocity, $u_\tau = \sqrt{\frac{\tau_w}{\rho}}$
w [m·s^{-1}]	Vertical velocity component
y^+ [–]	Wall normal distance, in wall units: $y^+ = y\,u_\tau/\nu$

Dimensionless numbers

Pe [–]	Peclét number, Eq. (5)
Pr [–]	Prandtl number, Eq. (5)
Re [–]	Reynolds number, Eq. (5)
Ri [–]	Richardson number, Eq. (5)

Greek symbols

α [K^{-1}]	Volumetric thermal expansion coefficient of water
β [–]	Quantifies non-ideal behaviour of THS (see Eqs. (11a) and (11b))
γ [–]	Ratio of mass-flow rate of secondary with primary circuit
μ [kg·m^{-1}·s^{-1}]	Dynamic viscosity of water
μ_t [kg·m^{-1}·s^{-1}]	Turbulent viscosity (see, e.g., Pope [17])
μ_{eff} [kg·m^{-1}·s^{-1}]	$\mu + \mu_t$
Ω [s^{-1}]	Characteristic mean rotation rate (see, e.g. Pope [17])
Π^* [–]	Non-dimensional, gauge pressure, Eq. (3)
ρ [kg·m^{-3}]	Density of water
τ_w [Pa]	Wall shear stress
ϑ [–]	Non-dimensional temperature, Eq. (3))

Vectors

$\boldsymbol{g}$ [m·s^{-2}]	Gravitational acceleration vector
$\boldsymbol{u}$ [m·s^{-1}]	Velocity vector
$\boldsymbol{x}$ [m]	Position vector

Subscripts

0	Reference (pressure, temperature) conditions
b	Mass-flow averaged (*bulk*) quantity
t	Identify quantities somehow related to the axial direction of the THS

Superscript

$*$	Non-dimensional quantities, Eq. (3)

1. Introduction

Thermo-hydraulic separators (THSs) are flow collectors of relatively small size, connecting two or more hydraulic networks. They are designed to attain the hydraulic mutual independence of the connected circuits. Several technical reports from manufacturers claim that thermal-hydraulic separators improve the operation of thermal-hydraulic networks under different respects [6,5]: the heat supply to the end users is more stable and the secondary circulating pumps are less prone to failure due to off-design operation or to the onset of intense inrush currents during repeated starts under high back-pressure. The hydraulic separation of primary from secondary circuits reduces the pumping power ascribed to the main circulating pump, which has to overcome only the head loss through the primary network. When the primary network is connected to a heat source, a constant flow rate can be maintained throughout the boiler, which is therefore protected from overheating during modulations of the heat rejection to the end users [22]. THSs may also integrate the functions of degassing, sludge removal and removal of ferromagnetic debris [6,5].

Different devices can be used to hydraulically separate connected hydraulic networks [6]. Closely-space tees provide a low-cost alternative to THSs: nevertheless, the limited diameter of the connecting branch might induce a significant head loss through the primary and secondary circuits. The plate heat exchangers feature a high heat transfer efficiency (usually higher than 90%): they separate physically the connected networks, but are expensive and require constant maintenance to keep them clean from fouling.The storage tanks are large fluid containers, used for thermal water heating storage and distribution. The connected circuits are hydraulically separated and benefit from the large thermal inertia of the tank, which nevertheless imposes long pre-heating periods whenever the plant have to be restarted. None of the aforementioned alternatives to the THSs have the inherent capability of removing gas and sediments.

THSs are often used as thermo-hydraulic dispatchers in heat supply systems: the hot/cold water supplied to the THS by the heating/cooling plant (heat source (HS)) is transferred to one or more heat exchange networks (heat consumer (HC)). Yan et al. [23] compare district heating systems with distributed variable speed pumps (DVSP-DH) and with a conventional central circulating pump (CCCP-DH), respectively. In DVSP-DH systems the primary and secondary circuits are linked by hydraulic dispatchers. In DVSP-DH networks, a pump is installed at each substation of the secondary network: the control valves, used to distribute the flow among substations in CCCP-DH systems become therefore unnecessary. This, in turn, induces significant energy savings, as the power loss related to the throttling is avoided. Yan et al. [23] report that substituting a CCCP-DH system with a DVSP-DH system in a district heating plant in Kuerle, China, resulted in a reduction of pumping power from 238 kW to 194 kW and in about 30% energy saving under changing flow rates of one or several consumers.

Yavorovsky et al. [24] investigate by numerical simulation the flow

and temperature distribution inside two different types of THSs. The reported results provide evidence that, for the considered THS configurations, the temperature of the fluid supplied to the HC is significantly independent both of the flow rate through the HS and of the ratio γ between the flow rates of secondary to primary circuits.

Yavorovsky et al. [25] report on a combined experimental and numerical investigation on a THS, confirming that the connected secondary circuits are hydraulically separated from each other.

Anisimova [1] investigates by numerical simulation a THS connected to a horizontal collector supplying four different heat consumers. The reported results provide evidence of a significant deviation of the THS from the expected behavior, in terms of supply/return temperatures.

A recent experimental and numerical study by Romanov and Yavorovsky [19] compares the temperature drop from HS to HC for both the in-line and the staggered connection of the manifolds.

The present, numerical investigation reveals the flow and temperature distributions within the THS and assesses the reliability of a widely used design model, hereafter referred to as 0D model. The 0D model represents a THS as a double-T junction, where the flow along the connecting branch is unidirectional and recirculates the excess flow rate of the HS circuit. This idealized model disregards the turbulent and molecular mixing of heat and momentum, the thermally-induced convection, the presence of additional fluid streams caused by the three-dimensionality of the flow.

2. Materials and methods

2.1. About the considered device

A THS consists of a tank, mostly of cylindrical shape, endowed with two or more couples of connecting pipes. The present investigation focuses on the geometry sketched in Fig. 1a, where the following geometrical aspect ratios are used:

$$D/d = 3, \quad H/d = 6$$

The device is limited above and below by two spherical cap lids with radius of curvature 5d. The THS links one HS to one HC. A typical installation in a heating plant is shown in Fig. 1b: the THS connects the supply and return manifolds with a limited pressure loss. The connecting pipes are identified as reported in Table 1 and shown in Fig. 1a. It is assumed that the lateral surface of the THS is perfectly thermally-insulated (THSs are usually enclosed in a layer of insulating material).

Table 1
Naming conventions of connecting pipes.

1:	BIP (Boiler Inlet Pipe)	Into THS from HS.
2:	PIP (Plant Inlet Pipe)	From THS to HC.
3:	POP (Plant Outlet Pipe)	Into THS from HC.
4:	BOP (Boiler Outlet Pipe)	From THS to HS.

A mass flow rate $\dot{m}$ of water flows through the HS, while a mass flow rate $\gamma\,\dot{m}$, with $\gamma \leqslant 1$, flows through the HC. The operative condition $\gamma > 1$ corresponds to inverting the roles of the HS and of the HC.

2.2. Governing equations

Water is the working fluid, assumed incompressible and Newtonian. The relative thermal expansion of the fluid is $\alpha\,\Delta T$~0.005 at 338.15 K (65 °C), when assuming a reference ΔT of 10 K: thus, the Boussinesq approximation is invoked [14]. Consistently, the viscous heating is neglected. With the aforementioned assumptions, the mass-, momentum- and energy-conservation equations result in:

$$\nabla\cdot\boldsymbol{u} = 0 \tag{1a}$$

$$\rho_0 \frac{\mathrm{D}\boldsymbol{u}}{\mathrm{D}t} = -\nabla P + \mu_0\,\Delta\boldsymbol{u} - \rho_0\,\alpha_0\,(T - T_0)\boldsymbol{g} \tag{1b}$$

$$\rho_0\,c_0 \frac{\mathrm{D}T}{\mathrm{D}t} = k_0\,\Delta T \tag{1c}$$

where P denotes the *gauge* pressure, i.e., the static pressure p reduced by the hydrostatic contribution:

$$P \equiv p - \rho_0\,\boldsymbol{g}\cdot\boldsymbol{x} \tag{2}$$

The 0 subscript identifies the reference conditions.

The physical quantities involved in fluid flow and heat transfer are made non-dimensional using the following *scales*: the diameter d of the connecting pipes, the mean inflow velocity U through the BIP, the temperature decay $\Delta T \equiv (T_2 - T_3)$ throughout the HC. The ensuing non-

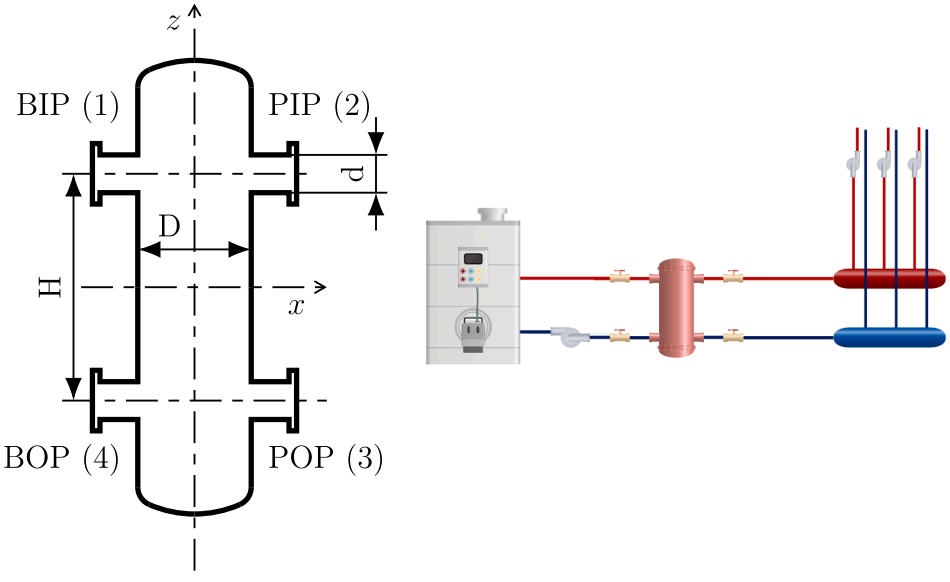

(a) Sketch of the considered THS on the symmetry plane $y = 0$.

(b) Typical installation of a THS in a heating plant.

Fig. 1. (a) Geometric configuration and (b) typical installation of a THS.

dimensional groups are formed:

$$\begin{aligned} \boldsymbol{x}^* &\equiv \frac{\boldsymbol{x}}{d} & t^* &\equiv \frac{t\,U}{d} \\ \boldsymbol{u}^* &\equiv \frac{\boldsymbol{u}}{U} & \Pi^* &\equiv \frac{P+\rho_0\alpha_0\boldsymbol{g}\cdot\boldsymbol{x}\,(T_1-T_0)}{\rho_0 U^2} \\ \vartheta &\equiv \frac{T_1-T}{\Delta T} \end{aligned} \tag{3}$$

The resulting, non-dimensional governing equations are:

$$\nabla^*\cdot\boldsymbol{u}^* = 0 \tag{4a}$$

$$\frac{\mathrm{D}\boldsymbol{u}^*}{\mathrm{D}t^*} = -\nabla^*\Pi^* + \frac{1}{Re}\Delta^*\boldsymbol{u} + Ri\,\vartheta\,\frac{\boldsymbol{g}}{g} \tag{4b}$$

$$\frac{\mathrm{D}\vartheta}{\mathrm{D}t^*} = \frac{1}{Pe}\Delta^*\vartheta \tag{4c}$$

The parameters Re, Ri and Pe are the well-known dimensionless groups Reynolds, Richardson and Péclet, respectively:

$$Re \equiv \frac{\rho_0\,U\,d}{\mu_0};\quad Ri \equiv \frac{g\,\beta_0\,\Delta T\,d}{U^2};\quad Pe \equiv \frac{U\,d}{\alpha_0} \tag{5}$$

The conditions enforced on the boundaries of the computational domain are summarized in Table 2: they introduce the flow ratio γ as an additional parameter. The dimensionless pressure, velocity and temperature depend on position $\boldsymbol{x}^*$ and time t^*, on the Reynolds, Richardson and Péclet numbers and on the mass-flow ratio γ:

$$\boldsymbol{u}^*,\ \Pi^*,\ \vartheta = f(\boldsymbol{x}^*,\ t^*,\ Re, Ri,\ Pe,\ \gamma) \tag{6}$$

2.3. Thermal model for THSs

The *ideal* flow distribution within a THS is schematically represented in Fig. 2, for $\gamma \leqslant 1$. Both turbulent mixing and thermal diffusion are assumed negligible. The bulk fluid temperatures at the inflow/outflow open boundaries are derived from mass and energy conservation:

$$T_2 = T_1 \ \text{ or } \ \vartheta_2 = \vartheta_1 \tag{8a}$$

$$T_3 = T_2 - \Delta T \ \text{ or } \ \vartheta_3 = 1 \tag{8b}$$

$$T_4 = T_1 - \gamma\,\Delta T \ \text{ or } \ \vartheta_4 = \gamma \tag{8c}$$

Eqs. (8a) and (8c) describe the *ideal* operation mode of a THS (0D model), not accounting for parasitic streams from the POP towards the PIP or for heat transfer within the device by turbulent mixing or molecular diffusion. Consequently, the temperature of the water remains constant as it flows from BIP to PIP (Eq. (8a)).

Under ideal working conditions, a representative *mixing cup* temperature T_b for the THS can be defined as the bulk temperature of the outflow streams:

$$T_b \equiv \frac{T_4 + \gamma T_2}{1+\gamma} \tag{9}$$

or, equivalently:

$$\vartheta_b = \frac{\gamma}{1+\gamma} \tag{10}$$

We aim to identify the range of the aforementioned dimensionless groups in practical applications. To this end, let's assume to use DN 50 (2 inches) connection pipes, with interior diameter d~54 mm, U~2 m/s, $\Delta T = 10$ K and $T_1 = 343.15$ K(70 °C). The bulk temperature T_b lies in a narrow range between 338.15 K(65 °C) and 340.15 K(67 °C) when γ decreases from 1 to 0.5. Evaluating all thermophysical properties of water at 339.15 K(66 °C), the Prandtl number Pr is 2.57, while the Richardson number is $Ri \approx 7\times10^{-4}$: both groups are kept constant in the reported simulations. Four different Reynolds numbers are considered, namely Re = 20000, 74145, 128290 and 256580. They correspond to practical applications where hot water is supplied to the THS through a DN50 pipe at velocity of 0.17 m/s, 0.65 m/s, 1.12 m/s and 2.25 m/s, respectively.

An alternative definition of the Richardson number Ri_t is based on the longitudinal velocity U_t of the descending flow stream, directed from the BIP towards the BOP for $\gamma < 1$, and on the vertical distance H between the upper and lower connecting pipes:

$$U_t \equiv \frac{(1-\gamma)\dot{m}}{\rho\,\pi\,D^2/4} = U\left(\frac{d}{D}\right)^2(1-\gamma);\quad Ri_t = \frac{g\alpha\Delta T H}{U_t^2}$$

Ri_t grows unbounded for $\gamma \to 1$, as for such limiting condition there is no transverse flow throughout the barrel. Assuming $\gamma = 0.75$, Ri_t is 799.3, 54.7, 18.4, 4.6 when Re = 20000, 74145, 128290, 256580: this suggests that natural convection effects within the barrel cannot be underestimated.

An unfavorable operation condition occurs whenever a fraction β of the flow returning from the HC is recirculated from port 3 to port 2. Satisfying the mass and energy conservation principles, while taking into account the constraint (7 h), the mass flow rates and the fluid temperatures can be derived at each open boundary of the THS, as reported in Table 3 and represented in Fig. 3. The actual values of ϑ_2 and ϑ_3 can be used as indicators of the deviation from the expected behavior of the THS. The value of ϑ_4 is independent of the operating mode of the THS and results solely from a global energy balance. It is worth stressing that the aforementioned *phenomenological* model accounts only for the presence of a *parasitic* stream, while it does not consider the turbulent and the molecular diffusion of heat between the ascending (*parasitic*) and the descending streams. As a consequence, β itself may be interpreted just as a rough indication of the relative intensity of the parasitic flow. Nevertheless, the parameter β returns the actual temperatures ϑ_2 and ϑ_3 through Eqs. (11a) and (11b), which may be interpreted as indirect *definitions* of β. The parameter β ranges from $\beta = 0$ - ideal behaviour - to $\beta = 1$: the latter value corresponds to conditions where the HS and HC circuits recirculate their own working fluid, in turn implying $\vartheta_2 = \vartheta_3$.

2.4. Numerical model

The governing equations, reported in Section 2.2, are solved with the commercial finite-volume model ANSYS Fluent® 18.1.0. The Reynolds-Averaged-Navier-Stokes (RANS) approach is pursued, where the Reynolds stresses are represented via the $k-\varepsilon$ RNG model [17]. In principle, the $k-\varepsilon$ RNG model can deal with streamline curvature, swirl and rapid strain (see Appendix A) and is reasonably computationally efficient, requiring the solution of only two additional partial differential equations. The $k-\varepsilon$ RNG model is validated against experimental data by Yavorovsky et al. [24] for a model of THS bearing some similarities with that considered in the present work (see Appendix C). Further details about the turbulence modelling used in this work are provided in Appendix A.

The advective fluxes of all transported quantities through the faces of the computational control volumes are approximated by the second-

Table 2
Boundary conditions for Eqs. (1) and (4).

Boundary	Type	Flow		Heat transfer	
Walls	No-slip, adiabatic	$\boldsymbol{u} = 0$ $\boldsymbol{u}^* = 0$	(7a)	$\nabla T\cdot\boldsymbol{n} = 0$ $\nabla^*\vartheta\cdot\boldsymbol{n} = 0$	(7b)
BIP	Mass-flow inlet	$\dot{m}_1 = \dot{m}$ $\dot{m}_1^* = 1$	(7c)	T_1 $\vartheta_1 = 0$	(7d)
PIP	Pressure outlet	$p_2 = 0$ $\Pi_2^* = 0$	(7e)	$\nabla T\cdot\boldsymbol{n} = 0$ $\nabla^*\vartheta\cdot\boldsymbol{n} = 0$	(7f)
POP	Mass-flow inlet	$\dot{m}_3 = \gamma\cdot\dot{m}$ $\dot{m}_3^* = \gamma$	(7g)	$T_3 = T_2 - \Delta T$ $\vartheta_3 = \vartheta_2 + 1$	(7h)
BOP	Mass-flow outlet	$\dot{m}_4 = \dot{m}$ $\dot{m}_4^* = 1$	(7i)	$\nabla T\cdot\boldsymbol{n} = 0$ $\nabla^*\vartheta\cdot\boldsymbol{n} = 0$	(7j)

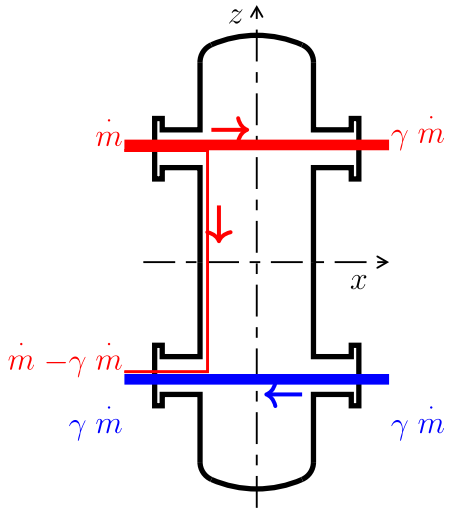

Fig. 2. Sketch on the symmetry plane $y = 0$ of the ideal working conditions of a THS ($\gamma \leqslant 1$). Red lines denote hot water coming from HS to HC, whilst blue ones represent cold water flowing from HC to HS. The labels identify the mass flow rates of the different streams. (For interpretation of the references to color in this figure legend, the reader is referred to the web version of this article.)

Table 3
Flow ratio $\dot{m}^*$ (i.e., mass flow rate scaled by the mass flow rate through the BIP) and dimensionless fluid temperature at each open boundary of the THS, under non-ideal working conditions.

Open boundary	Flow ratio $\dot{m}^*$	Temperature ϑ	
BIP	1	0	
BOP	1	γ	
PIP	γ	$\frac{\beta}{1-\beta}$	(11a)
POP	γ	$\frac{1}{1-\beta}$	(11b)

order upwind scheme: the value of the advected quantity on the face of a computational cell is approximated by a linear Taylor expansion based on the centroid of the upstream cell. The gradient of the transported quantity, required for the aforementioned Taylor expansion, is reconstructed by a linear least-squares approach and limited by a scalar minmod limiter function to prevent the onset of spurious oscillations near local rapid changes in the flow field [8,3]. Mass fluxes across control volume faces are calculated by a variant of the procedure proposed by Rhie and Chow [18], to avoid the *checkerboarding* effect due to the co-located variable arrangement [21]. The momentum and continuity equations are decoupled with two iterations of neighbor and skewness correction of the PISO scheme [8]. The $RNG - k\varepsilon$ model does not provide enough turbulent viscosity, to entirely damp the turbulence fluctuations in the reported sumulations. Therefore, unsteady-RANS (URANS) simulations are carried out, starting from a flow field obtained by solving a potential-flow problem and from an isothermal temperature field (temperature taken from the inlet boundary condition enforced at BIP). The simulation is then carried on for the time required to twice evacuate the fluid contained within the device (two *flow-through times*), in order to attain statistically-steady conditions. The simulation is then continued for three flow-through times to acquire the statistics, representative of the regime operation of the device. During this stage, the maximum value of the Courant-Friederich-Levy (CFL) number oscillates about 1.0. A first-order implicit time-stepping scheme is used to advance the solution during the initial, transitory phase, while a second-order implicit time-stepping scheme is applied during the statistically-steady data-accumulation stage.

Unstructured, polyhedral meshes are generated by the open-source package snappyHexMesh [22]. The mesh used for the reported calculations encompasses approximately 0.7 million cells: the surface-averaged, wall-normal distance of the cell centroid nearest to the wall, for the case with $Re = 20000\,(256580)$ and $\gamma = 1$, is $y_1^+ = 12.1\,(23.8)$ wall units, with a corresponding standard deviation $\sigma_{y_1^+} = 1.98\,(17.0)$.

During each time-step, the residuals of all the governing equations are scaled with the maximum of the corresponding residuals within the first five iterations: the iterative solution of the discretized equations is continued until all *scaled* residuals drop by a factor of at least 10^{-3}. It was verified that further reducing the scaled residuals by an order of magnitude does not significantly affect the results.

Results of a mesh-sensitivity study are reported in Appendix B. The proposed numerical model is validated by comparison against experimental data available in [25] (Appendix C).

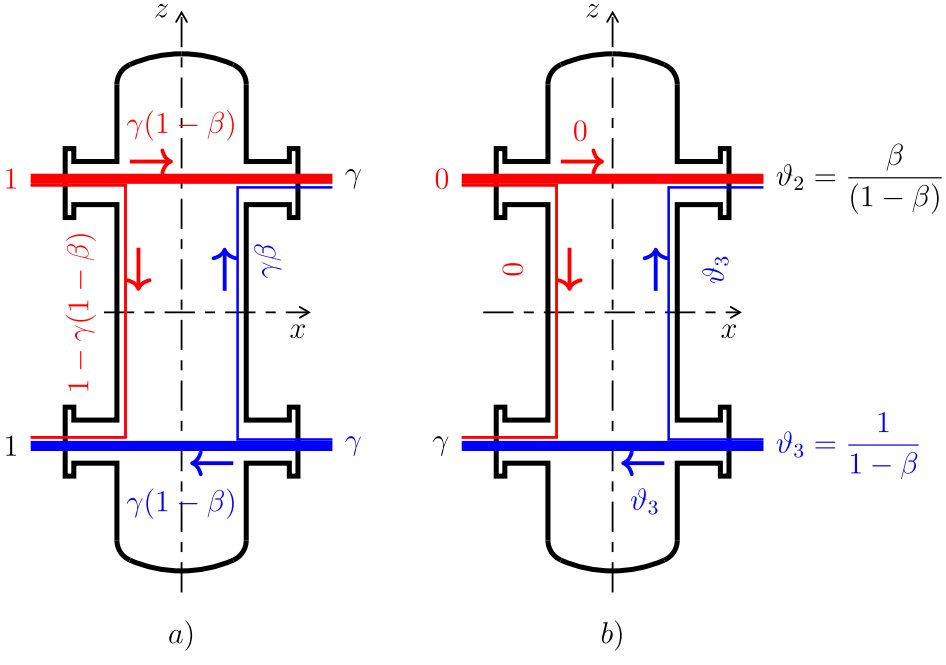

Fig. 3. Sketch on the symmetry plane $y = 0$ of the non-ideal working conditions of a THS. (a) Mass fluxes; (b) temperature.

3. Results

3.1. Flow field

Fig. 4 shows several streamlines on the (x, z) symmetry plane of the device, for two cases with $Re = 128290$ and $\gamma = 0.5$ or $\gamma = 1.0$. The streamlines are superimposed to a contour plot of the dimensionless temperature ϑ. For both cases, the upper- and the lower-most regions of the THS are interested by recirculation bubbles, where the fluid tends to stagnate. The most striking differences between the two cases occur in the central part of the barrel: for $\gamma = 0.5$ the flow recirculated to the primary circuit tends to *squeeze* against the HC-side of the barrel's wall while moving downwards. The fluid cools down progressively, due to the mixing induced by the secondary motions developing on the $y - z$ plane (see Fig. 5). For $\gamma = 1$, the central part of the THS is interested by a recirculation bubble, which drags and mixes fluid from the supply (*warm*) and return (*cold*) streams. Consequently, the temperature of the fluid supplied to the HC is lower than expected, motivating the relatively low values of β for $\gamma = 1$ (see Fig. 10).

The time-averaged streamlines in the y-z plane are shown in Fig. 5: the flow pattern reveals several counter-rotating, secondary vortices that contribute to the convective mixing within the device.

Fig. 6 reports the distribution of the vertical velocity w^* on the symmetry plane $y^* = 0$ of the device, with low supply flow rate ($Re = 20000$). The pattern of w^* obtained with high flow rate is qualitatively similar. It is evident that upward-/ downward-oriented streams develop due to the impact of the two main streams against the wall of the separator. This suggests that designing smoother entry sections of the outflow pipes could represent a viable option to reduce the extent of the vertical flow and the ensuing mixing within the THS.

Depending on the Reynolds number and on the value of γ, the regions of high turbulence intensity are located either within the mixing layers surrounding the main streams, or within the wall jet resulting from the impact of the supply flow (entering through the BIP) against the case of the THS (marked WJ1 in Fig. 7c), or within the *impact zones* surrounding the POP and BOP (marked SI1 and SI2 in Fig. 7c).

Isosurfaces corresponding to TI = 10% are shown in Fig. 7 for $\gamma = 0.5$ and $\gamma = 1.0$, for $Re = 20000$ while for $Re = 256580$ they are shown for TI = 30%. In the ensuring discussion, the term "isosurface" denotes the isosurface TI = 10% for $Re = 20000$ and TI = 30% for $Re = 256580$ respectively. For $\gamma = 0.5$ the isosurface lies in the wall jet WJ1 and only for $Re = 256580$, in the regions SI1 and SI2. For $\gamma = 1.0$, the wall jet region WJ1 is absent, as there is no excess flow recirculating from the BIP towards the BOP. For $Re = 20000$, the isosurface does not extend into the barrel, while for $Re = 256580$ most the turbulence is located within the impact regions SI1 and SI2. The region SI2 is not clearly discernible in the case $Re = 256580$ with $\gamma = 0.5$, due to the reduced mass flow rate flowing from the POP towards the BOP.

The turbulent intensity, volume-averaged within the barrel, is represented in Fig. 8: it lies in the range 1.8–2.5% and 11.6–15.6% for $Re = 20000$ and $Re = 256580$, respectively. The turbulence intensity increases with Re within the considered range, with a weak inversion for Re in the intermediate range 74145–128290. TI shows a weaker dependence on γ: except for γ approaching 1.0, a decreasing trend with γ is evident for all Reynolds numbers. The isosurfaces reported in Fig. 7 give some clue to interpret the trend of TI shown in Fig. 8. For $Re = 20000$, the turbulence intensity diminishes monotonically with increasing γ due to the decreasing extension of the region WJ1. This is not the case for the higher Reynolds numbers, where the shrinkage of the WJ1 region with increasing γ is partially compensated by the widening of the region SI2. The high turbulence intensity registered in the impact regions SI1 and SI2 suggests that smoothing out the entrance of PIP and BOP could be a reasonable approach to reduce the overall turbulence intensity within the THS, in turn extending the range of suitable Reynolds numbers for the primary flow.

The total pressure loss $\Delta\Pi^*_{tot}$ induced by the THS on the primary and secondary networks is shown in Fig. 9. $\Delta\Pi^*_{tot}$ is calculated between two cross-flow sections located 1d upstream from the inlet port and 1d downstream to the outlet port. $\Delta\Pi^*_{tot}$ does not show a strong dependence on the Reynolds number in the considered range. The pressure loss is higher for the HS than for the HC circuit and both tend to decrease with increasing γ: the hydraulic separation of the connected circuits is better accomplished when γ is close to 1.0. $\Delta\Pi^*_{tot}$ may be interpreted as half of a concentrated pressure-loss coefficient. For $\gamma = 0.5$ the THS behaves as

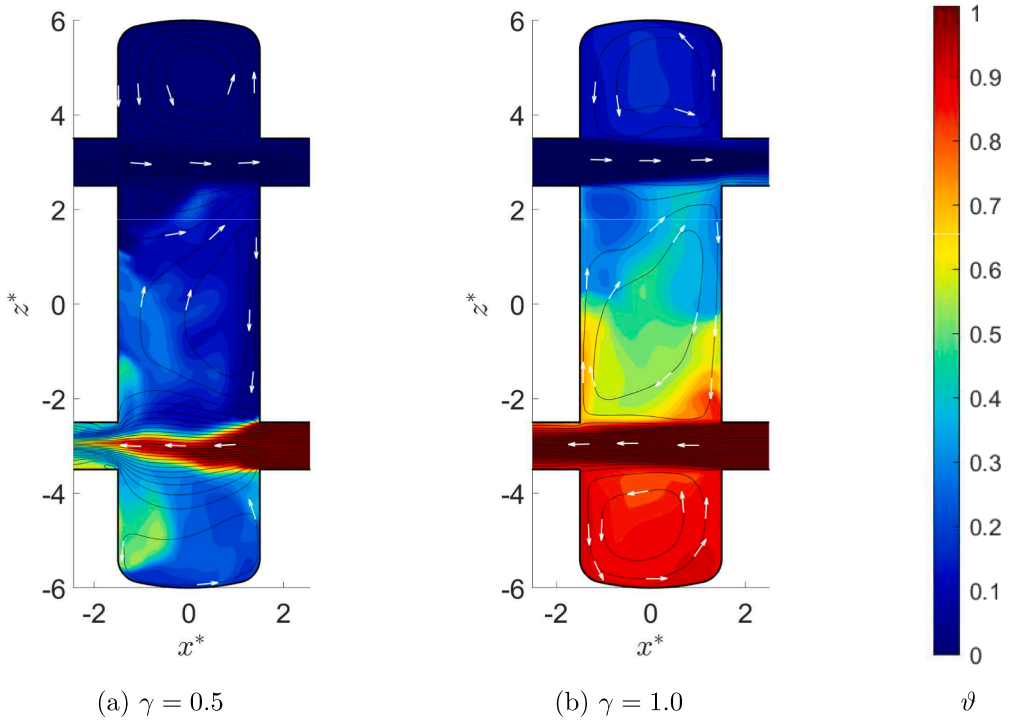

Fig. 4. Streamlines on the (x^*, z^*) symmetry plane of the device ($y^* = 0$), superimposed to the contour plot of ϑ. (a) $Re = 128290$, $\gamma = 0.5$; (b) $Re = 128290$, $\gamma = 1.0$.

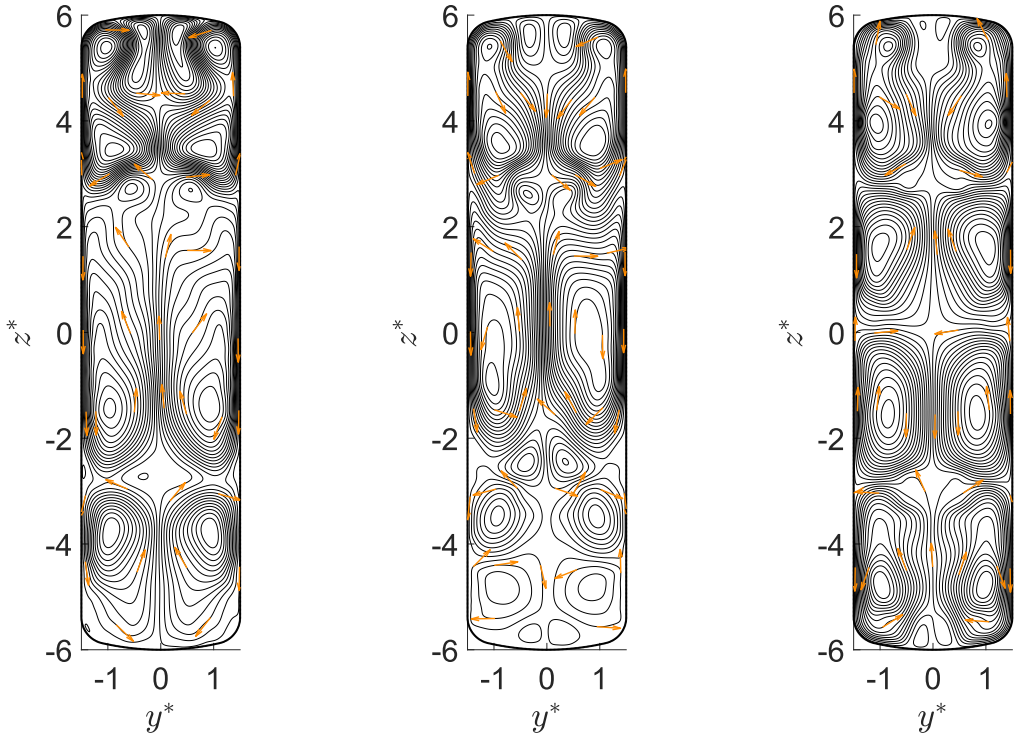

(a) $\gamma = 0.5$ (b) $\gamma = 0.7$ (c) $\gamma = 1.0$

Fig. 5. Streamlines on the (y^*, z^*) cut-plane of the device ($x^* = 0$) for $Re = 128290$.

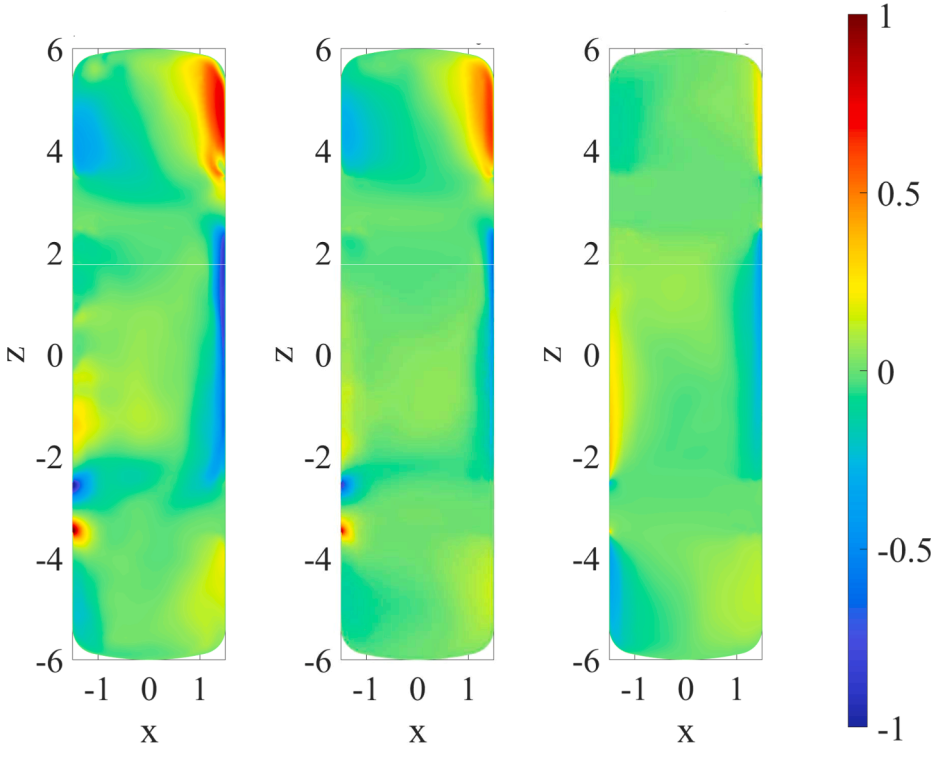

(a) $\gamma = 0.5$ (b) $\gamma = 0.7$ (c) $\gamma = 1.0$ w^*

Fig. 6. Contour of w^* on the symmetry plane $y^* = 0$. $Re = 20000$.

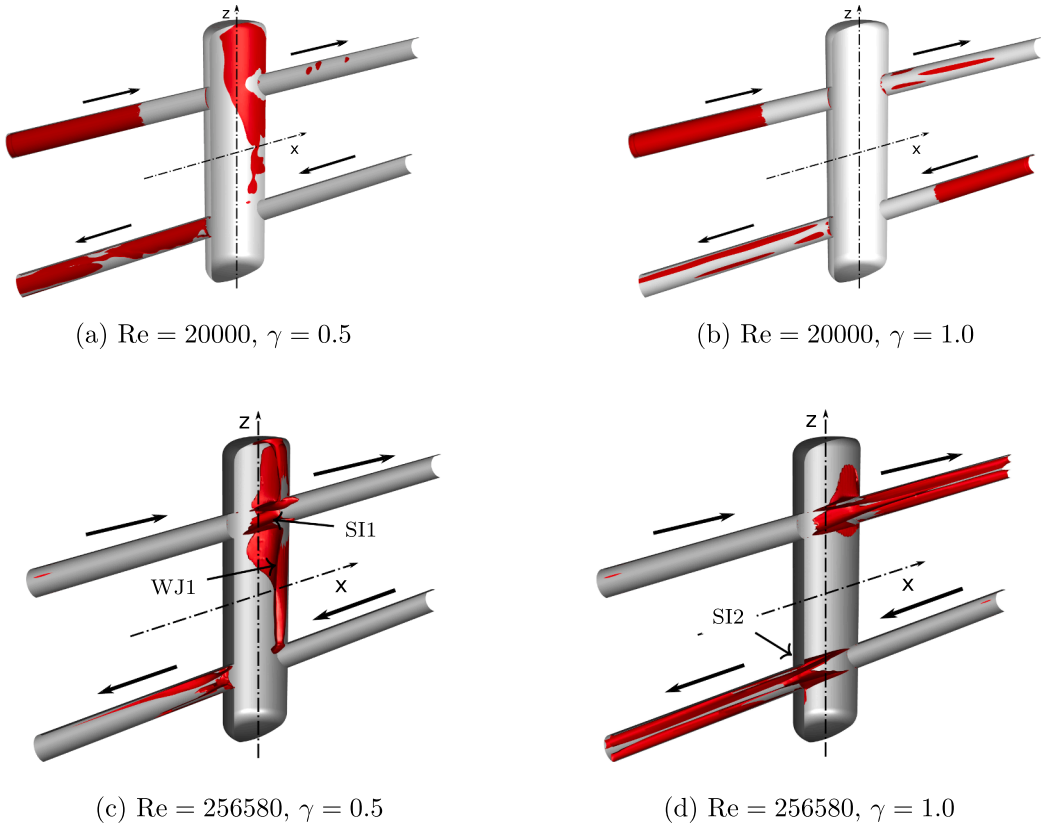

(a) Re = 20000, $\gamma = 0.5$ (b) Re = 20000, $\gamma = 1.0$

(c) Re = 256580, $\gamma = 0.5$ (d) Re = 256580, $\gamma = 1.0$

Fig. 7. Isosurface TI = 10% for $Re = 20000$ and isosurface TI = 30% for $Re = 256580$. The device is sectioned on the symmetry plane $y = 0$.

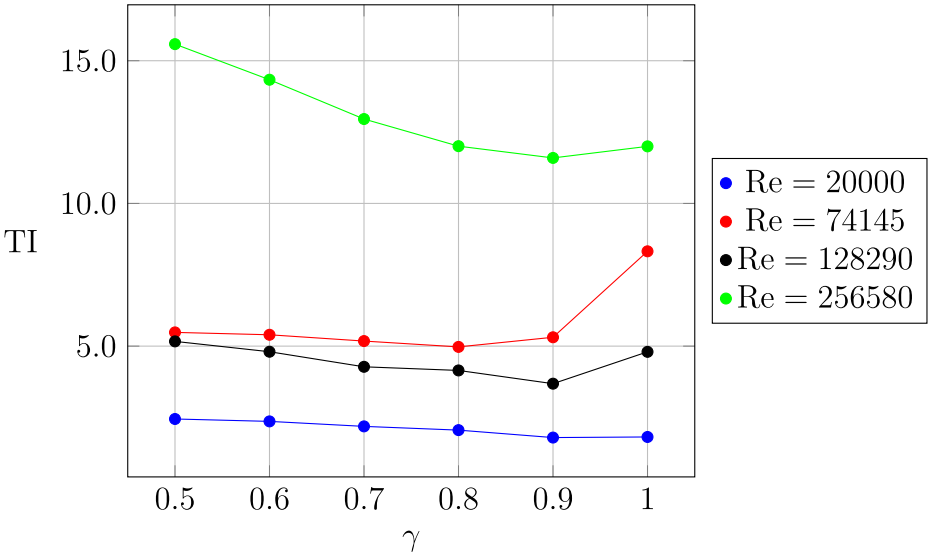

Fig. 8. Mean TI within the THS.

a butterfly valve with 20° or 10° closure on the HS and HC circuits, respectively [10].

3.2. Assessment of the 0D thermal model of THSs

The parameter β, reported in Table 4, provides a second-order approximation (in β) to ϑ_2, which in turn gives the temperature loss from the BIP to the PIP scaled by the temperature drop through the HC network. The parameter β increases monotonically both with γ and with Re, due to the increased mixing induced by the recirculation bubble for the largest values of γ (see Section 3.1) and by the turbulent fluctuations when rising *Re*. This trend is violated for $Re = 74145$ and $\gamma = 0.5$ and $\gamma = 0.6$, where higher-than-expected values of β are obtained. This feature is consistent with the relatively high level of turbulence intensity recorded for this intermediate Reynolds number (see Fig. 8). From the viewpoint of practical applications, these values of β are yet of negligible relevance and the 0D model is still very accurate. Fig. 10 represents the temperature loss at the PIP entrance, for a temperature drop across the HC of 10 K. The supply temperature to the HC decreases with increasing γ and with increasing Reynolds. Considering the worst condition, where $\gamma = 1$, the supply temperature to the HC drops by 0.24 K and 0.49 K with respect to the boiler supply

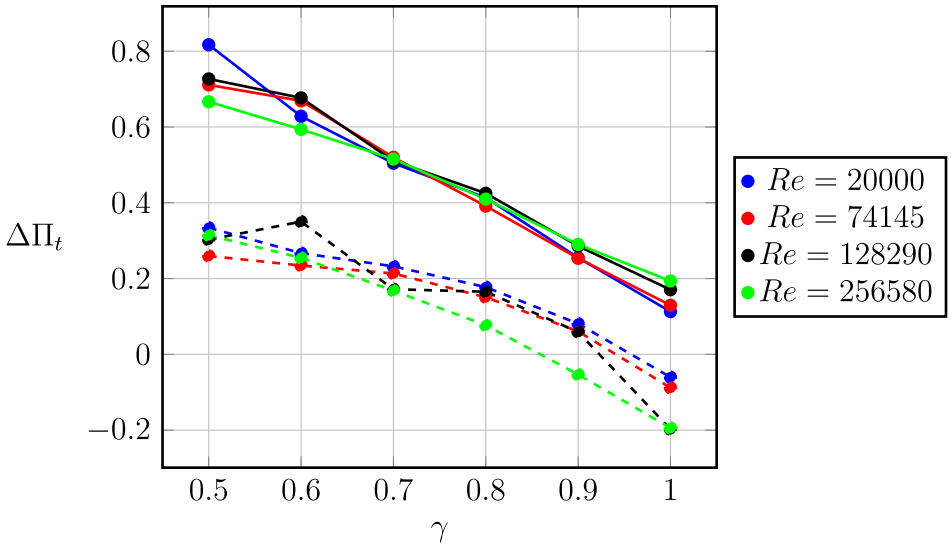

Fig. 9. Drop in total pressure between BIP and BOP (solid line) and between POP and PIP (dashed line), respectively.

Table 4
Values of β depending on Re and γ.

γ	Reynolds			
	20000	74145	128290	256580
0.5	0.00030254	0.0033298	0.00083215	0.00025397
0.6	0.00067144	0.003549	0.00085582	0.0015329
0.7	0.00094320	0.0014953	0.0014832	0.0037833
0.8	0.00206010	0.002716	0.0017358	0.0072806
0.9	0.00237480	0.0031543	0.0057318	0.017707
1.0	0.02306000	0.030342	0.040289	0.046585

temperature, for the lowest and highest considered Reynolds numbers, respectively.

3.3. Thermal stratification within the separator

In principle, the flow field inside a THS should be thermally stratified, in order to reduce the heat exchange between the warm stream, coming from the HS, and the cold stream, stemming from the HC. A *stratification index*, SI, is proposed, to quantify the thermal stratification within the device:

$$\mathrm{SI} \equiv \frac{\vartheta_4 - \vartheta_2}{\vartheta_b} \tag{12}$$

Under non-ideal operating conditions, the non-dimensional bulk temperature is given by:

$$\vartheta_b = \frac{1}{1-\beta}\frac{\gamma}{1+\gamma} \tag{13}$$

SI depends on γ and β as:

$$\mathrm{SI} = (1+\gamma)\left(1 - \beta\frac{1+\gamma}{\gamma}\right) \tag{14}$$

Complete mixing within the THS implies $\vartheta_b = \vartheta_4 = \vartheta_2 = \gamma$, SI = 0 and $\beta = \gamma/(1+\gamma)$. The temperature loss between BIP and PIP is $\gamma\,\Delta T$, under these conditions. We may conjecture that the flow within the THS is *perfectly* thermally stratified when $\vartheta_2 = 0$ (warm stream flowing from HS to HC without loosing heat) and $\vartheta_4 = 1$ (cold stream flowing from HC to HS without gaining heat). This condition is attained only when

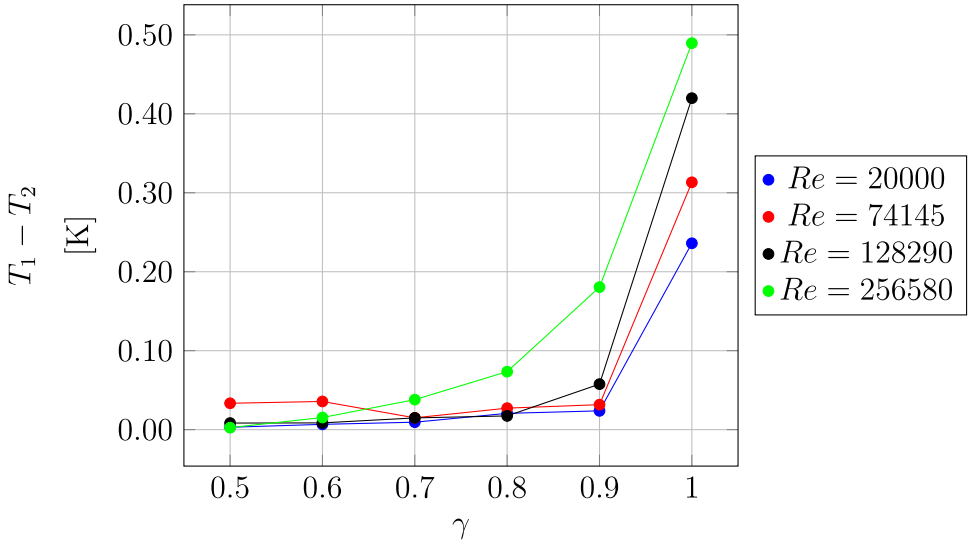

Fig. 10. Temperature loss at PIP due to non-ideal behavior of the THS, for a temperature drop across the HC of 10 K. Data are reported for different values of γ and for all considered Reynolds numbers.

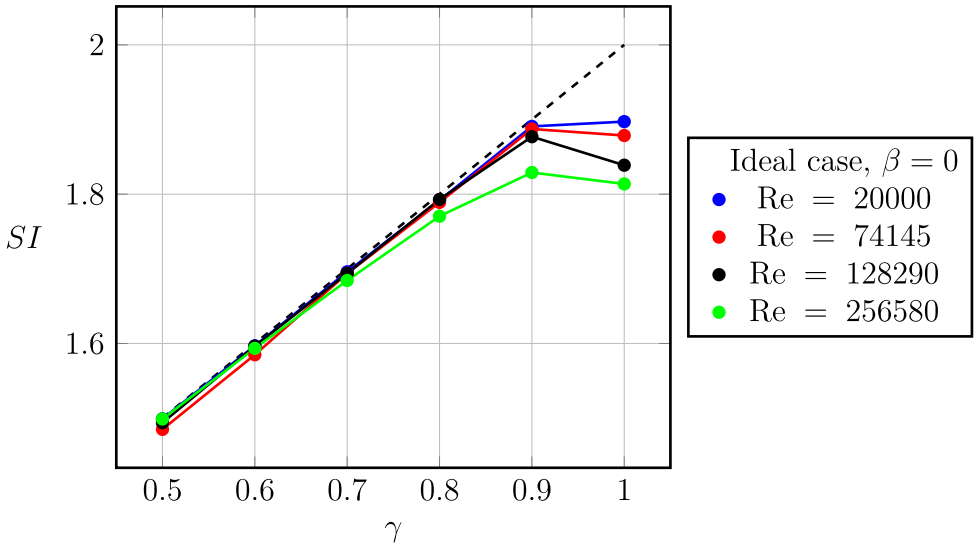

Fig. 11. Dependence of the stratification index SI on the flow ratio γ.

$\gamma = 1$ and $\beta = 0$, i.e. only for the ideal, on-design operation of the separator, condition for which $\vartheta_b = 0.5$ and SI = 2.

Fig. 11 shows the dependence of SI on γ. Thermal stratification increases with γ, as expected due to the corresponding weakening of the descending, warm stream from BIP towards BOP. This trend is inverted for $\gamma \gtrsim 0.9$, where a relatively large deviation from the expected behavior occurs: a reasonable interpretation is that the *parasitic* stream from POP towards PIP cools the *bypass* HS-to-HC stream, inducing an increment of ϑ_2. This effect is more pronounced at the highest considered Reynolds number.

Fig. 12 shows the profile of ϑ along the vertical axis of the THS. The *dead* zones occupying the uppermost and lowermost portions of the THS contain fluid at markedly different temperature from that of the adjoining, main streams, due to the fluid conveyed towards these regions by the secondary vortices shown in Fig. 5. For $\gamma < 1$ the temperature increases (correspondingly, ϑ decreases) gradually with z, due to the presence of the descending stream of warm fluid, which progressively cools down by loosing heat towards the surrounding fluid by turbulent and molecular thermal diffusion. For $\gamma = 1$ there is no descending stream: the core of the barrel is interested by a recirculation bubble at rather uniform temperature, intermediate between T_1 and T_3.

4. Concluding remarks

The flow and temperature pattern within a cylindrical thermal-hydraulic separator is investigated by numerical simulation. The

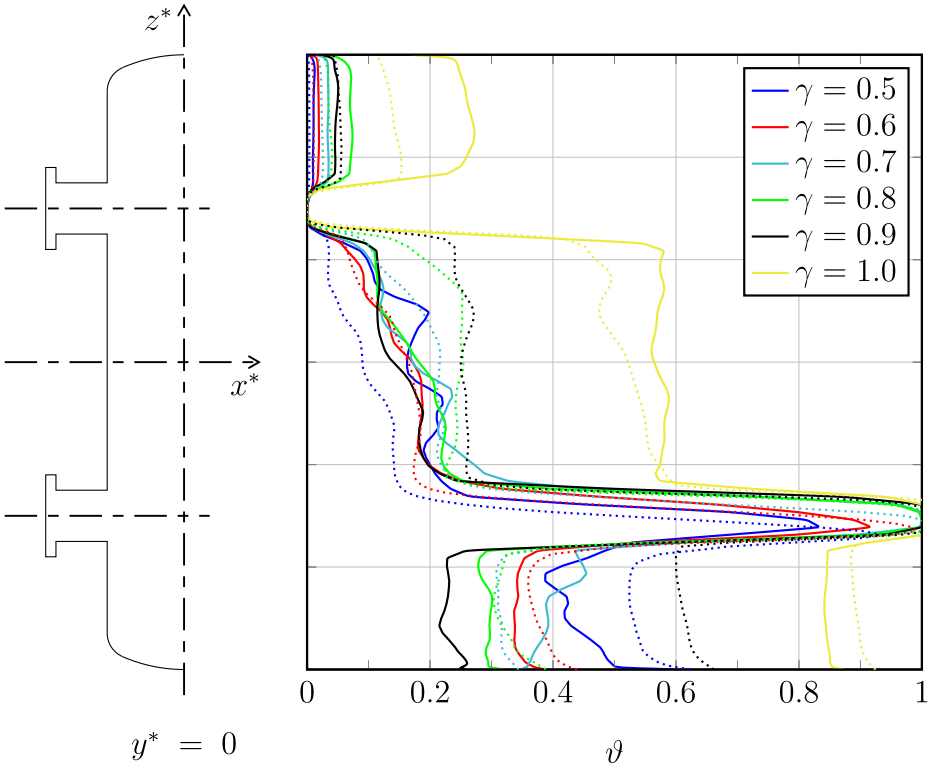

Fig. 12. Distribution of ϑ along the vertical axis z of the device. Solid lines: $Re = 20000$. Dotted lines: $Re = 256580$.

calculated temperature of the outflow streams is used to define a quantitative measure of the deviation of the *actual* behavior of the device from the expectations of a widely accepted theoretical model. The model assumes that the secondary circuit is not interested by fluid recirculation and that turbulent mixing and molecular diffusion are insignificant. All in all, the aforementioned model turns out to be highly reliable: the most significant deviation from the simulated results, quantified by the parameter β, occurs for a flow ratio $\gamma = 1.0$, i.e. same flow rate through the heat source and the heat consumer and for the highest considered Reynolds number. Under this condition a re-circulation bubble occupies the central part of the thermal-hydraulic separator and contributes to the heat exchange between the *main* supply- and return-streams. Secondary vortices are also identified on the cross-flow symmetry plane of the thermal-hydraulic separator for any considered value of γ: they also contribute to the mixing of the internal energy within the device.

Thermal stratification is often claimed to be a positive, yet qualitative, feature for a thermal-hydraulic separator device [25,19]. The proposed *stratification index* SI, Eq. (12), provides a quantitative estimate of the thermal stratification within the considered thermal-hydraulic separator and is related to the index β.

The considered thermal-hydraulic separator induces a pressure loss on both the primary and the secondary circuits, which increases when γ is reduced. For $\gamma = 0.5$ and $Re = 256580$, the thermal-hydraulic separator acts on the primary circuit as a butterfly valve, with approximately 20° closure. The proposed investigation strategy and the definition of the *quantitative* parameters β and SI can be applied to different models of thermal-hydraulic separators. The characterization of thermal-hydraulic separators connecting a number of heat consumers networks to the heat source (see, e.g. [25]) would possibly require to define more than a single parameter β, depending on several flow ratios γ, but the underlying idea of relating the simple, phenomenological model used for design purposes to the *true* behavior of a thermal-hydraulic separator, still applies.

Declaration of Competing Interest

The authors declare that they have no known competing financial interests or personal relationships that could have appeared to influence the work reported in this paper.

Appendix A. Turbulence model

Turbulence is resolved by the Reynolds Averaged Navier Stokes (RANS) approach: the governing equations are averaged over time and the time-averaged flow quantities, from here on identified by an overline, become the dependent variables [17]. The non-linear terms in the time-averaged governing equations give rise to a *closure problem*, as turbulent stresses $-\rho_0 \overline{\boldsymbol{u}'\boldsymbol{u}'}$ and turbulent heat fluxes $-\rho_0 c_0 \overline{\boldsymbol{u}' T'}$ must be somehow related to the time-averaged flow quantities:

$$\nabla\cdot\overline{\boldsymbol{u}} = 0 \tag{A.1a}$$

$$\rho_0 \frac{\mathrm{D}\overline{\boldsymbol{u}}}{\mathrm{D}t} = -\nabla\overline{P} + \mu_0 \Delta\overline{\boldsymbol{u}} - \rho_0 \beta_0 (\overline{T} - T_0)\boldsymbol{g} + \nabla\cdot(-\rho_0 \overline{\boldsymbol{u}'\boldsymbol{u}'}) \tag{A.1b}$$

$$\rho_0 c_0 \frac{\mathrm{D}\overline{T}}{\mathrm{D}t} = k_0 \Delta\overline{T} + \nabla\cdot(-\rho_0 c_0 \overline{\boldsymbol{u}' T'}) \tag{A.1c}$$

The turbulent stresses are linked to the time-averaged velocity by an eddy viscosity model [17]:

$$-\rho_0 \overline{u_i' u_j'} = \mu_t [\overline{u}_{i,j} + \overline{u}_{j,i}] \tag{A.2}$$

The turbulent viscosity μ_t is prescribed according to the RNG-k $-$ ε model, which is based on the statistical technique known as *Renormalization Group Theory* [16]. In principle, for the present application the RNG-kε model bears several advantages over other two-equation models: the model is free of adjustable parameters and can be applied for modeling both fully-developed turbulence and low-Reynolds flows. The effective-viscosity ratio $\hat{\nu} \equiv \frac{\mu_{eff}}{\mu}$ comes from the solution of an ordinary differential equation (*differential viscosity model*). The differential viscosity model is claimed to better handle low-Reynolds number flows and near-wall flows [2], while in the limit of large Reynolds numbers, where $\mu_t \gg \mu$, it returns the classical relation $\mu_t = C_\mu k^2/\varepsilon$, with $C_\mu = 0.0845$ very close to the classical value of $C_\mu = 0.09$ used in the standard $k - \varepsilon$ model.

The turbulent viscosity is then modified to account for the effect of intense swirl, correcting thereof a known inconsistency of eddy-viscosity models that makes them insensitive to the streamline curvature and to the system rotation [20]: $\mu_t = \mu_{t0} f(\alpha_s, \Omega, k/\varepsilon)$. The swirl constant α_s is set to 0.07, suitable for mildly swirling flows.

The turbulent kinetic energy k and the turbulent energy dissipation ε are solutions of two additional transport equations [16]:

$$\rho_0 \frac{\partial\overline{k}}{\partial t} + \rho_0 \frac{\partial}{\partial x_j}(\overline{k}\,\overline{u}_j) = \frac{\partial}{\partial x_j}\left(\alpha_k \mu_{eff} \frac{\partial\overline{k}}{\partial x_j}\right) + G_k + G_b + -\rho_0 \overline{\varepsilon} \tag{A.3a}$$

$$\rho_0 \frac{\partial\overline{\varepsilon}}{\partial t} + \rho_0 \frac{\partial}{\partial x_j}(\overline{\varepsilon}\,\overline{u}_j) = \frac{\partial}{\partial x_j}\left(\alpha_\varepsilon \mu_{eff} \frac{\partial\overline{\varepsilon}}{\partial x_j}\right) + C_{1\varepsilon} \frac{\overline{\varepsilon}}{\overline{k}}(G_k + C_{3\varepsilon} G_b) + -C_{2\varepsilon} \rho_0 \frac{\overline{\varepsilon}^2}{\overline{k}} - R_\varepsilon \tag{A.3b}$$

Differently from other $k - \varepsilon$ models, Eq. (A.3b) is not purely empirical: instead, it is derived from the Navier-Stokes equations using the re-normalization-group theory. According to RNG theory, $C_{1\varepsilon} = 1.42$ and $C_{2\varepsilon} = 1.68$. G_k represents the production of turbulent kinetic energy due to the mean velocity gradients and, as for the standard $k - \varepsilon$ model, this term does not give rise to an additional closure problem:

$$G_k = -\rho_0 \overline{u_i' u_j'} \frac{\partial\overline{u}_j}{\partial x_i} = \mu_t S^2 \tag{A.4}$$

where the modulus S of the mean rate-of-strain tensor is defined as

$$S = \sqrt{2 S_{ij} S_{ij}}; \quad S_{ij} \equiv \frac{1}{2}\left[\bar{u}_{i,j} + \bar{u}_{j,i}\right] \tag{A.5}$$

G_b is the generation of turbulent kinetic energy due to buoyancy. R_ε is an additional term in the ε equation, not present in the standard $k-\varepsilon$ model and not derived from RNG theory [17], which tends to increase $\bar{\varepsilon}$ in regions of rapid strain (turbulence to mean shear time scale ratio $Sk/\varepsilon \gg 3-6$), reducing $\bar{k}$ and μ_t [17]:

$$R_\varepsilon = \frac{C_\mu \eta^3 \left(1 - \frac{\eta}{\eta_0}\right)}{1 + \beta \eta^3} \cdot \frac{\varepsilon^2}{k} \tag{A.6}$$

R_ε makes the RNG model more responsive to the effects of rapid strain and streamline curvature than the standard $k-\varepsilon$model, making it a good candidate for the modeling of turbulence in the present flow configuration, in particular within the regions where the main streams bend sharply upon impacting against the barrel's wall. η attains values of about 45 when $Re = 256580$ and $\gamma = 1$. The quantities α_k and α_ε are the inverse effective Prandtl numbers for $\bar{k}$ and $\bar{\varepsilon}$, respectively: they are derived analytically from the RNG theory as

$$\left|\frac{\alpha - 1.3929}{\alpha_0 - 1.3929}\right|^{0.6321} \left|\frac{\alpha + 2.3929}{\alpha_0 + 2.3929}\right|^{0.3679} = \frac{\mu}{\mu_{eff}}; \quad \alpha_0 = 1 \tag{A.7}$$

The turbulent heat flux vector is modeled by an eddy-diffusivity approach, relying on the definition of an effective thermal conductivity k_{eff} and of a turbulent Prandtl number σ_T:

$$-\rho_0 c_0 \overline{u_i' T'} = k_{eff} \frac{\partial \bar{T}}{\partial x_i} \tag{A.8}$$

where k_{eff} is the *effective* thermal conductivity, related to the turbulent viscosity and to the turbulent Prandtl number σ_T:

$$k_{eff} = \frac{c_0 \mu_{eff}}{\sigma_T} \tag{A.9}$$

σ_T is calculated from (A.7) using $\alpha = \frac{1}{\sigma_T}$ and $\alpha_0 = 1/Pr$. This is another positive feature of the RNG-$k\varepsilon$ model when non-isothermal flows are concerned: the turbulent Prandtl number does not need to be specified as a further adjustable parameter.The buoyancy contribution G_b to the generation of k is, under the Boussinesq assumption:

$$\begin{aligned} G_b &= -\rho_0 \alpha g_i \overline{u_i' T'} \\ &= (\alpha g_i) \frac{\mu_{eff}}{Pr_t} \frac{\partial \bar{T}}{\partial x_i} \end{aligned} \tag{A.10}$$

The buoyancy term becomes a sink of turbulent kinetic energy in stably-stratified turbulence. The term G_b appears also in the transport equation for ε, pre-multiplied with a coefficient $C_{3\varepsilon}$ given by [11]:

$$C_{3\varepsilon} = \tanh\left|\frac{v}{u}\right|$$

where v is the component of the flow velocity parallel to the gravitational vector and u is the component of the flow velocity perpendicular to the gravitational vector.

The boundary conditions at solid walls are enforced using the wall function approach proposed by Launder and Spalding [15]. The tangential velocity profile throughout the turbulent boundary layer is given by the *law of the wall* [17]:

$$\bar{u}_P = \frac{u_\tau^2}{u_P^*} \begin{cases} \frac{1}{\kappa} \log(E y_P^*); & y_P^* \geqslant 11.225 \\ y_P^*; & y_P^* < 11.225 \end{cases} \tag{A.11}$$

where the relevant velocity scales in the near-wall region are taken as

$$u_\tau \equiv \sqrt{\frac{\tau_w}{\rho}}; \quad u_P^* \equiv C_\mu^{1/4} \sqrt{k_P}; \quad C_\mu = 0.09 \tag{A.12}$$

and the non-dimensional wall-normal distance y_P^* is defined as

$$y_P^* \equiv y_P \frac{u_P^*}{\nu} \tag{A.13}$$

Based on experimental evidence the velocity scale u^* approximates the friction velocity u_τ but can be calculated more easily in numerical simulations. The empirical constants E and κ (the von Karman constant) are assigned as

$$E = 9.793; \quad \kappa = 0.4187 \tag{A.14}$$

Eq. (A.11) links the wall shear stress to the mean velocity at the closest node to the wall. In turn, the wall shear stress provides dynamical boundary conditions for the momentum equations.

The wall-function approach is pursued for the energy equation as well. Eq. (A.11) is adapted to represent the temperature variation within the thermal boundary layer according to the Reynolds' analogy concept [12]:

$$\bar{T}_w - \bar{T}_P = T^* \begin{cases} Pr_T \left[\frac{1}{\kappa} \log(E y_P^*) + P\right]; & y_P^* \geqslant y_T^* \\ Pr\, y_P^*; & y_P^* < y_T^* \end{cases} \tag{A.15}$$

where $Pr_T = 0.85$ and y_T^* is the non-dimensional, wall-normal distance at which the two profiles are crossing. T^* denotes the so-called *friction*

temperature, defined as $T^* = \frac{q_w''}{\rho} c_p u_t$ where q_w'' is the heat flux at the wall. The correction term P is suggested by Jayatillika [13]:

$$P \equiv 9.24\left[\left(\frac{Pr}{Pr_T}\right)^{3/4} - 1\right][1 + 0.28\mathrm{e}^{-0.007 Pr/Pr_T}] \tag{A.16}$$

The wall-function approach outlined above is modified according to the *scalable wall-function* philosophy [9], consisting in limiting the minimum value of y_P^* to 11.225 to improve the results in conditions where y_P^* is not consistently larger than 11.225 throughout the whole mesh.

The conservation equations for k and ε have to be constrained by proper boundary conditions. At the mass-flow inlet boundaries, BIP and POP, the turbulence intensity TI and the hydraulic diameter D_h are assigned. The following empirical correlation, valid for fully-developed duct flows, is used to identify physically realistic values of TI [2, Eq. (6.68)]:

$$\mathrm{TI} = 0.16(Re_{D_h})^{-1/8} \tag{A.17}$$

At the PIP and BOP boundaries, where mass-flow outlet and pressure-outlet conditions hold, respectively, both k and ε are extrapolated from the interior of the computational domain. TI from Eq. (A.17) and D_h are assigned at the BOP boundary in the case of reverse flow.

The mixing-length hypothesis is invoked in order to derive ε from k and D_h. The *turbulent length scale* l and the *turbulent mixing length* l_m are defined as:

$$l = \frac{k^{3/2}}{\varepsilon}; \quad l_m = C_\mu^{3/4} l \tag{A.18}$$

l is related to the size of the largest turbulent eddies: for a fully-developed turbulent duct flow the following empirical correlation is used:

$$l_m = 0.07 D_h \tag{A.19}$$

The turbulent dissipation at the I/O boundaries is obtained from (A.18):

$$\varepsilon = C_\mu^{3/4} \frac{k^{3/2}}{l_m} \tag{A.20}$$

At the solid walls, the zero-gradient boundary condition applies for the turbulence kinetic energy

$$\left.\frac{\partial k}{\partial n}\right|_w = 0 \tag{A.21}$$

The assumption (A.21) is reasonable as k is known to vary as y^{+2} in the viscous sublayer [4].

The turbulence dissipation is assigned at the first interior cell node, denoted by P, in accordance with the local-equilibrium assumption between turbulence production and turbulence dissipation within the logarithmic layer. Experimental evidence suggests that in the fully-turbulent region of a zero-pressure gradient boundary layer the turbulent shear stress is approximately constant and equal to the wall shear stress:

$$u_\tau^2 \equiv \frac{\tau_w}{\rho} \approx -\overline{u\,v} \tag{A.22}$$

Furthermore, in the same flow region the experimental evidence shows that

$$\sqrt{C_\mu} \equiv -\frac{\overline{u\,v}}{k} \approx \text{const.} \tag{A.23}$$

where $C_\mu \approx 0.09$. Combining (A.22) and (A.23) yields

$$k \approx \frac{u_\tau^2}{\sqrt{C_\mu}} \tag{A.24}$$

The local-equilibrium assumption states that, in the near-wall region of a turbulent boundary layer, outside the viscous sublayer, the transport terms in the conservation equation of k are relatively small, with the consequence that the production P_k of k and dissipation ε are in approximate balance:

$$\varepsilon \approx P_k = -\overline{u\,v}\frac{\partial U}{\partial n} \tag{A.25}$$

The gradient of the mean velocity is calculated from the logarithmic law of the wall:

$$\frac{\partial U}{\partial n} = \frac{u_\tau}{\kappa y} \tag{A.26}$$

Thus, the turbulent dissipation at the first interior node is

$$\varepsilon_P \approx P_{kP} \approx u_\tau^2 \frac{u_\tau}{\kappa y_P} = \frac{C_\mu^{3/4} k_P^{3/2}}{\kappa y_P} \tag{A.27}$$

Appendix B. Verification through Grid Independence Analysis

The mesh size for the reported simulations is chosen by a sensitivity analysis: simulations with progressively increasing mesh resolution are carried out for the configuration with $\gamma = 0.7$ and $Re = 128290$. The relative error on the mean turbulent kinetic energy $\overline{k}$ and the mean internal energy content $\overline{\vartheta}$ of the fluid within the separator are calculated on each mesh and reported in Table B.5. Table B.6 reports some quality indicators for the three considered meshes. The aforementioned errors are calculated with respect to a reference solution, derived by the Richardson extrapolation method with automatic identification of the order of the leading error term [7]. The error on the turbulent kinetic energy is scaled with the volume-averaged value of $\overline{k}$ arising from Richardson

Table B.5
Error on $\overline{k}$ and $\overline{e}$ with increasing mesh resolution. N denotes the number of cells. δ_{min} and $\overline{\delta}$ denote the minimum and mean *diameter* of a cell, respectively, computed as six times the ratio of the cell volume to cell face area, scaled by the diameter of the BIP. Richardson extrapolation is based on δ_{min}.

Mesh	N	δ_{min}	$\overline{\delta}$	Relative error on	
				$\overline{k}$ (%)	$\overline{e}$ (%)
A	376329	0.0071	0.11	14.9	1.1
B	780815	0.0053	0.084	1.61	0.863
C	2354647	0.0032	0.057	0.0349	0.0871

Table B.6
Quality indicators for mashes A, B, C.

MESH	Min. Orth. Qual	Max Asp. Ratio	Volume-averaged cell-equiangle skew	Min. y+	Max y+	Surface-averaged y+
A	0.051	2939	0.039	0.94	135.8	18.7
B	0.027	45.9	0.030	0.51	113.2	15.8
C	0.062	32.0	0.020	0.63	86.8	13.0

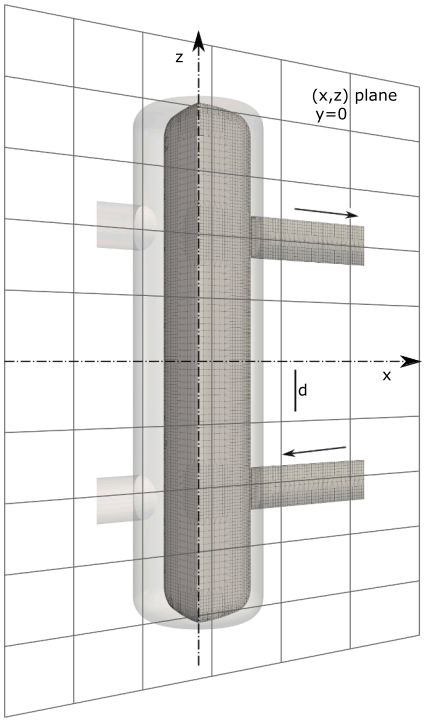

Fig. B.13. A quarter section of the mesh used for the simulations of the THS.

extrapolation, while the absolute error on $\overline{\vartheta}$ is not scaled as, by itself, it expresses the error on the volume-averaged internal energy of the fluid scaled by the jump in the internal energy of the fluid throughout the secondary circuit. Mesh B yields a reasonable compromise between accuracy and computing time and is therefore used for the present investigation: a cross-section of this mesh is shown in Fig. B.13.

Appendix C. Validation of the proposed numerical model

The reliability of the adopted numerical model is assessed by comparison against the experimental data by Yavorovsky et al. [25]. Yavorovsky et al. [25] carry out an experimental and numerical investigation of a THS. The considered THS can be connected to two primary and two secondary

Table C.7
Comparison of simulated non-dimensional temperatures with the corresponding experimental measurements by Yavorovsky et al. [25] (in brackets). T_1 and T_3 are enforced as boundary conditions: therefore, only T_2 and T_4 have to be compared.

Case	T_1 [K]	T_2 [K]	T_3 [K]	T_4 [K]	ε_{T_2} (%)	ε_{T_4} (%)
1	323.36	324.74 (323.25)	303.53	307.44 (306.07)	7.52	6.90
2	321.80	322.77 (321.68)	300.29	303.07 (303.07)	5.08	7.63

circuits. An electric boiler (primary circuit) provides hot water to the THS, which in turn feeds two HCs (secondary circuits), whose *active* elements are a heat exchanger and a radiator. As for the present validation, only the heat exchanger is connected to the THS. The outflow temperatures T_2 and T_4, measured by Yavorovsky et al. [25] using resistance thermometers, are compared in Table C.7 against the results, obtained with the present numerical model, while T_1 and T_3 are enforced as boundary conditions. The mass flow ratio γ is 0.877. The corresponding, relative, percent errors ε_{T_2} and ε_{T_4} are defined as

$$\varepsilon_{T_k} = 100\,\frac{T_{k,num} - T_{k,exp}}{T_1 - T_3} \qquad \text{with } k = 2 \text{ or } k = 4 \tag{C.1}$$

The present model is in reasonably good agreement with the experimental data by Yavorovsky et al. [25] under different operating conditions, with relative errors of ~6% − ~7%.

References

[1] E. Yu Anisimova, Improvement of decentralized heat supply systems, IOP Conf. Ser. Mater. Sci. Eng. 451 (2018) 012090. ISSN 1757-899X. doi: 10.1088/1757-899X/451/1/012090.

[2] ANSYS Fluent User's Guide, Release 19.0. ANSYS Inc., 2018.

[3] T.J. Barth, D. Jespersen, The design and application of upwind schemes on unstructured meshes, Technical report, AIAA, 1989.

[4] Jonas Bredberg, On the Wall Boundary Condition for Turbulence Models, 2000.

[5] Separatore Idraulico, CALEFFI, 2010. https://www.caleffi.com/sites/default/files/file/01076_it.pdf.

[6] Hydraulic Separation, Beyond Primary/ Secondary Piping, CALEFFI Hydronic Solution, 2007. URL https://www.caleffi.com/sites/default/files/file/hydraulicseparation-tr07.pdf.

[7] J.H. Ferziger, Numerical methods for engineering applications, second ed., Wiley Interscience, 1998. doi: 10.1007/978-3-642-56026-2.

[8] J.H. Ferziger, M. Perić, R.L. Street, Computational Methods for Fluid Dynamics, fourth ed., Springer International Publishing, Berlin, 2020, https://doi.org/10.1007/978-3-319-99693-6.

[9] B.M. Ginting, Central-upwind scheme for 2d turbulent shallow flows using high-resolution meshes with scalable wall functions, Comput. Fluids 179 (2019) 394–421, https://doi.org/10.1016/j.compfluid.2018.11.014.

[10] Don W. Green, Robert H. Perry, Perry's Chemical Engineers' Handbook, eighth ed., McGraw-Hill Education, New York, 2008, 1997, 1984, 1973, 1963, 1950, 1941, 1934. ISBN 9780071422949. https://www.accessengineeringlibrary.com/content/book/9780071422949.

[11] R.A.W.M. Henkes, F.F. van der Flugt, C.J. Hoogendoorn, Natural convection flow in a square cavity calculated with low-reynolds-number turbulence models, Int. J. Heat Mass Transf. 34 (1991) 1543–1557, https://doi.org/10.1016/0017-9310(91)90258-G.

[12] F.P. Incropera, D.P. DeWitt, Fundamentals of Heat and Mass Transfer, fourth ed., John Wiley & Sons, Inc., New York City, New York, 1996.

[13] C.L.V. Jayatillika, The Influence of Prandtl Number and Surface Roughness on the Laminar Sublayer to Momentum and Heat Transfer (PhD thesis), Imperial College, Mech. Eng. Dept., 1966. Rept. TWF/R/2.

[14] P.K. Kundu, I.M. Cohen, D.R. Dowling, Fluid Mechanics. Science Direct e-books, Elsevier Science, 9780123821003, 2012.

[15] B.E. Launder, D.B. Spalding, The numerical computation of turbulent flows, Comput. Methods Appl. Mech. Eng. 3 (1974) 269–289, https://doi.org/10.1016/0045-7825(74)90029-2.

[16] S.A. Orszag, V. Yakhot, W.S. Flannery, F. Boysan, D. Choudhury, J. Maruzewski, B. Patel, Renormalization group modeling and turbulence simulations, International Conference on Near-Wall Turbulent Flows, Tempe, AZ (USA), 1993.

[17] S.B. Pope, Turbulent Flows, Cambridge University Press, Cambridge (UK), 2000.

[18] C.M. Rhie, W.L. Chow, Numerical study of the turbulent flow past an airfoil with trailing edge separation, AIAA J. 21 (1983) 1525–1532, https://doi.org/10.2514/3.8284.

[19] D.O. Romanov, Y.V. Yavorovsky. Investigation of thermohydraulic dispatcher properties and peculiarities, in: E3S Web of Conferences, vol. 124, EDP Sciences, Oct 2019. doi: 10.1051/e3sconf/201912401009.

[20] P.R. Spalart, M. Shur, On the sensitization of turbulence models to rotation and curvature, Aerosp. Sci. Technol. 1 (5) (1997) 297–302, https://doi.org/10.1016/S1270-9638(97)90051-1 https://www.scopus.com/inward/record.uri?eid=2-s2.0-0031483314&doi=10.1016%2fS1270-9638%2897%2990051-1&partnerID=40&md5=45b7896c2f031590a4ba85a2797fb8ff. cited By 427.

[21] P. Vesseling, Principles of Computational Fluid Dynamics. Springer Series in Computational Mathematics, Springer, Berlin, 2001 10.1007/978-3-642-05146-3.

[22] H.G. Weller, H.J. Tabor, C. Fureby, A tensorial approach to computational continuum mechanics using object-oriented techniques, Comput. Phys. 12 (6) (1998) 193–321, https://doi.org/10.1063/1.168744.

[23] A. Yan, J. Zhao, Q. An, Y. Zhao, H. Li, Y.J. Huang, Hydraulic performance of a new district heating systems with distributed variable speed pumps, Appl. Energy 112 (2013) 876–885, https://doi.org/10.1016/j.apenergy.2013.06.031.

[24] Y.V. Yavorovsky, D.O. Romanov, V.V. Sennikov, I.A. Sultanguzin, A.S. Malenkov, E. V. Zhigulina, and A.V. Lulaev, Application of thermohydraulic dispatcher in low temperature district heating systems for decreasing heat carrier transportation energy cost and increasing reliability of heat supply, vol. 891, 2017. doi: 10.1088/1742-6596/891/1/012167.

[25] Y.V. Yavorovsky, D.O. Romanov, V.G. Khromchenkov, Experimental research of thermo-hydraulic separators and dispatchers in heat supply systems, Solid State Phenom. 284 (2018) 1385–1389, https://doi.org/10.4028/www.scientific.net/SSP.284.1385.